Applied Energy 354 (2024) 122262

Contents lists available at ScienceDirect

Applied Energy

journal homepage: www.elsevier.com/locate/apenergy

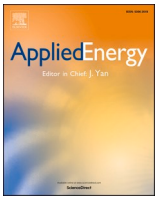

Dramatic mitigation of capacity decay and volume variation in vanadium redox flow batteries through modified preparation of electrolytes

F. Toja [a,*], L. Perlini [a], D. Facchi [b], A. Casalegno [a], M. Zago [a]

[a] Politecnico di Milano, Department of Energy, Via Lambruschini 4, 20156 Milano, Italy
[b] Solvay Specialty Polymers S.p.A., Viale Lombardia 20, 20021, Bollate, Milano, Italy

HIGHLIGHTS

- 1.6 M $V^{3.5+}$ in 2 M H_2SO_4 electrolyte induces capacity decay and volume variation.
- Initial capacity decay is caused by H^+ concentration gradient across the membrane.
- Capacity decay is mitigated by increasing H^+ concentration at negative electrolyte.
- Increasing proton concentration reduces both capacity decay and volume variation.

ARTICLE INFO

Keywords:
Capacity decay
Electrolyte imbalance
Vanadium cross-over
Volume variation
VRFB

ABSTRACT

Electrolyte imbalance caused by the undesired vanadium-ions cross-over and water transport through the membrane is one of the main critical issues of vanadium redox flow batteries, leading to battery capacity loss and electrolytes volume variation. In this work, the evolution of discharged capacity and electrolyte volume variation were firstly investigated adopting commercial electrolyte for hundreds of charge-discharge cycles in vanadium redox flow batteries employing different membranes, varying thickness and equivalent weight. Subsequently, with the support of a 1D physics-based model, the origin of the main phenomena regulating capacity decay and volume variation has been identified and different modifications in the preparation of electrolytes have been proposed. Electrolytes characterized by an equal proton concentration between the two tanks at the beginning of cycling operation turned out to limit capacity decay, while increasing electrolyte proton concentration was effective also in the mitigation of volume variation. The most promising electrolyte preparation combined the effect of high proton concentration and null osmotic pressure gradient between the two tanks: compared to commercial electrolyte this preparation reduced the capacity decay from 47.7% to 20.9%, increased the coulombic efficiency from 96.2% to 98.9% and the energy one from 79.9% to 83.4%, and also implied a negligible volume variation during cycles. The effectiveness of this electrolyte preparation has been verified with different membranes, increasing the range of validity of the results, that could be thus applied in a real system regardless of the adopted membrane.

1. Introduction

Vanadium redox flow battery (VRFB) is a promising technology for stationary energy storage due to an independent energy-to-power ratio and a long cycle life [1–3]. However, some technological issues still hinder VRFB commercialization, among which the electrolyte imbalance caused by the undesired vanadium-ions cross-over and water transport through the membrane [4–7]. These phenomena result in battery capacity loss and electrolytes volume variation, that can be recovered with periodic re-balancing procedures [8–11] leading to increased operating and maintenance costs [12,13].

In the literature lot of effort has been dedicated to the analysis of ions and water crossover [14–21], whose comprehension is still not consolidated. For this reason, modelling analysis is fundamental to provide an insight into the origin of the above-mentioned issues [22]. Oh et al. [20] developed a detailed 3D water transport model, evidencing that water and vanadium ions transport across the separator are strictly related. However, the analysis is limited to one charge-discharge cycle. Dong et al. [23] developed and validated a lumped model to understand

* Corresponding author.
E-mail address: francesco.toja@polimi.it (F. Toja).

https://doi.org/10.1016/j.apenergy.2023.122262
Received 15 July 2023; Received in revised form 6 October 2023; Accepted 2 November 2023
Available online 9 November 2023

Nomenclature

List of symbols

a	Specific Area $[m^{-1}]$
A_{geo}	Geometric Area $[m^2]$
C	Concentration $[mol\,m^{-3}]$
Cap	Capacity $[C]$
D	Diffusivity $[m^2\,s^{-1}]$
F	Faraday's Constant $[C\,mol^{-1}]$
h_{ch}	Mass transport coefficient in the distributor channel $[m\,s^{-1}]$
i_v	Volumetric current density $[A\,m^{-3}]$
K	Kinetic constant $[m\,s^{-1}]$
l	Thickness $[m]$
N	Molar flux $[mol\,m^{-2}s^{-1}]$
$\dot{Q}$	Volumetric flow rate $[m^3s^{-1}]$
R	Universal gas constant $[J\,mol^{-1}K^{-1}]$
r_p	Pore radius $[m]$
RR	Reaction Rate $[mol\,m^{-3}s^{-1}]$
SA	Surface Area $[m^2kg^{-1}]$
SoC	Stare of Charge $[-]$
T	Temperature $[K]$
V_p	Porous volume $[m^3kg^{-1}]$

Greek symbols

α	Charge transfer coefficient $[-]$
Δt	Time step $[s]$
ΔV	Voltage $[V]$
ϵ	Porosity $[-]$
η	Overpotential $[V]$
σ	Conductivity $[S\,m^{-1}]$
ϕ	Potential $[V]$

Superscripts

b	Relative to the bulk electrolyte
ch	Relative to the distributor channel
ch,el	Relative to the channel-electrode interface
eff	Effective
el	Relative to the electrode domain
in	Relative to the inlet
L	Relative to the left boundary of the domain
m	Relative to the membrane domain
mem	Relative to the membrane domain
neg	Relative to the negative electrode
out	Relative to the outlet
pos	Relative to the positive electrode
R	Relative to the right boundary of the domain
s	Relative to the electrode surface

Subscripts

cx	Relative to cross-over
i	Relative to the species i
H^+	Relative to the H^+ species
HSO_4^-	Relative to the HSO_4^+ species
l	Relative to the electrolytic phase
neg	Relative to the negative electrode/electrolyte
pos	Relative to the positive electrode/electrolyte
s	Relative to the solid phase
SO_4^{2-}	Relative to the SO_4^{2-} species
t	Relative to the iteration t
V^{2+}	Relative to the V^{2+} species
V^{3+}	Relative to the V^{3+} species
VO^{2+}	Relative to the VO^{2+} species
VO_2^+	Relative to the VO_2^+ species

transport phenomena associated with capacity loss through a Nafion®115 membrane: proton transport turned out to be an important factor regulating capacity loss, since the imbalance in proton concentration can accelerate water transport through the membrane. Water transport has been extensively analysed by the research group of M.S. Kazacos. In [14] it was demonstrated that in cation exchange membranes a significant amount of water is transferred from the negative to the positive half-cell, while in [15] it was shown that the direction of preferential water transfer is dependent on the state of charge (SoC) of the vanadium electrolytes. However, in [14,15], the analyses were performed in an appositely developed test cell, that does not resemble an operating VRFB during charge-discharge cycles. All these works [14,15,20,23] highlighted the complexity of the involved phenomena and the importance of electrolyte composition in the evolution of capacity decay and water transport.

Recently, Shin et al. [24] proposed a new operating strategy to alleviate the electrolyte imbalance, which employs water and sulfuric acid at different concentrations between the negative and positive electrodes. However, the effectiveness of the proposed approach was only verified with the aid of a detailed 3D numerical model. In a later work, Shin et al. [25] validated experimentally the mitigation strategies, but the analysis was carried out just for one charge-discharge cycle and capacity decay along with battery efficiencies were not considered in the analysis. Also Wang et al. [26] and Chen et al. [27] modified the electrolyte composition to reduce electrolyte imbalance in VRFB. In [26] capacity decay was mitigated by increasing the average oxidation state of the electrolytes, while in [27] a reduction of both capacity decay and volume variation was obtained with the introduction of additives in the electrolytes. Anyway, in both these works the comprehension of the origin of the reduced capacity decay is not carefully explained. The literature still lacks works validating mitigation strategies with different membrane materials, analysing simultaneously the effect on volume variation, discharged capacity and battery efficiencies.

In this work, the evolution of discharged capacity and electrolyte volume variation were firstly investigated adopting a commercial electrolyte for hundreds of charge-discharge cycles in VRFBs employing different membranes, varying thickness and equivalent weight (EW). Subsequently, with the support of a 1D physics-based model, the origin of the main phenomena regulating battery capacity decay and volume variation has been identified and different modifications in the preparation of electrolytes have been proposed in order to mitigate the above-mentioned operating issues. The most promising electrolyte preparation methodology has been tested with all the membranes analysed in this work, increasing the range of validity of the results, that could be thus applied in a real system regardless of the adopted membrane.

The paper is organized as follows: the experimental hardware and tests are described in Section 2, and then, in Section 3, 1D model development is presented. Section 4 firstly presents experimental results with commercial electrolytes and modelling analysis highlighting the main governing physical phenomena. Subsequently, different electrolytes modifications are proposed and validated experimentally. Finally, some conclusions are given in Section 5.

2. Experimental

2.1. Experimental hardware

The VRFB cell active area was 25 cm^2 with interdigitated graphite distributors. Positive and negative electrode were carbon felt Sigracell® GFD 2.5 EA (nominal thickness 2.5 mm, compressed to 2 mm). Three Aquivion® membranes characterized by different thickness and equivalent weight (EW) were tested: E98–05 (thickness 50 μm, EW 980 g mol^{-1}), E87–05 (thickness 50 μm, EW 870 g mol^{-1}) and E98–09 (thickness 90 μm, EW 980 g mol^{-1}).

5 different electrolyte compositions were tested, each one obtained by solving vanadium (IV) sulfate oxide hydrate in an aqueous solution of sulfuric acid. For the sake of clarity, just the preparation of the reference commercial electrolyte is explained in paragraph 2.2, while all the other electrolyte modifications are clearly described in correspondence of the relative experimental characterization. In order to avoid air infiltration [28], the tanks containing the electrolyte were pressurized with N_2. A peristaltic pump (Watson Marlow 323 Du with a 314 Dw 4 roller head pump) was used to flow the electrolyte in the hydraulic circuit.

Charge-discharge cycles were performed with a Autolab PGSTAT 30® potentiostat by Metrohm with a 10 A booster module and SCAN250 module (DC potential accuracy ±0.2% f.s., DC current accuracy ±0.5% f.s).

Two webcams (Papalook 1080p PA452 Pro) were used to monitor electrolyte volume variation in the two tanks. The electrolytes volume was detected and quantified with empty hydraulic circuit at the beginning of the test, after the first cycle and then once a day. Moreover, during charge-discharge cycles electrolytes volume was acquired every five minutes.

2.2. Preparation of commercial electrolyte

The commercially available electrolyte found in the literature usually consists of an aqueous solution of 1.6 M vanadium ions dissolved in 2 M of sulfuric acid [29,30]. In particular vanadium ions are present as V^{3+} and V^{4+} in ratio 1:1, leading to an overall oxidation state equal to 3.5; this electrolyte solution is commonly named $V^{3.5+}$. Since the commercially available electrolyte presents a relatively high uncertainty in the concentration of vanadium and sulfuric acid [29,30], in this work it has been prepared starting from the dissolution of 1.6 M $VOSO_4$ (99.9% purity, Alfa Aesar) in an aqueous sulfuric acid solution of 2 M. In this way it is possible to have highly repeatable measurements and precise electrolyte modifications.

Firstly, three reservoirs with 65[1] ml of V^{4+} are prepared. Two reservoirs undergo a pre-charge phase: at the positive electrode V^{4+} is completely oxidized to V^{5+}, while at the negative one V^{4+} is completely reduced to V^{3+}. Then the reservoir containing V^{3+} is mixed with the one containing V^{4+}, obtaining a solution characterized by the same amount of V^{3+} and V^{4+} ions which reproduces the commercially available electrolyte found in the literature.

Before charge-discharge cycles, both battery tanks are filled with 50 ml of $V^{3.5+}$: at the positive electrode $V^{3.5+}$ is completely oxidized to V^{4+}, while at the negative one $V^{3.5+}$ is completely reduced to V^{3+}, following the reactions (1 and (2, respectively.

$$V^{3+} + H_2O \rightarrow VO^{2+} + 2H^+ + e^- \quad at\ (+) \tag{1}$$

$$VO^{2+} + 2H^+ + e^- \rightarrow V^{3+} + H_2O \quad at\ (-) \tag{2}$$

At the end of this process the battery is at a State of Charge equal to 0 and is ready to perform charge-discharge cycles.

[1] The electrolyte that undergoes the pre-charge phase is prepared with an excess of 15 ml in order to assure a volume of 50 ml at the beginning of the test.

2.3. Experimental tests

Capacity decay and electrolytes volume variation are evaluated during charge-discharge cycles at 0.1 A cm^{-2} with fixed cut-off voltages. The upper voltage limit is 1.65 V to avoid the occurrence of undesired hydrogen evolution [31–33] and positive electrode corrosion [34–36], while the lower one is fixed at 1 V. In between each charge and discharge phase the battery is kept for 90 s in open circuit condition and the open circuit voltage (OCV) is monitored. The overall duration of the charge-discharge cycles is 13 days. During all tests the volumetric flow rate of the electrolyte is 40 ml min^{-1}.

During charge-discharge cycles coulombic (η_C), voltage (η_V) and energy (η_E) efficiencies are estimated according to the following definitions:

$$\eta_C = \frac{\int^{t_{discharge}} I \cdot dt}{\int^{t_{charge}} I \cdot dt} \tag{3}$$

$$\eta_V = \frac{\frac{1}{t_{discharge}} \int^{t_{discharge}} \Delta V \cdot dt}{\frac{1}{t_{charge}} \int^{t_{charge}} \Delta V \cdot dt} \tag{4}$$

$$\eta_E = \frac{\int^{t_{discharge}} I \cdot \Delta V \cdot dt}{\int^{t_{charge}} I \cdot \Delta V \cdot dt} \tag{5}$$

Where I is the current, ΔV is the cell voltage, t_{charge} and $t_{discharge}$ are the duration of the cycle charge and discharge time respectively.

3. Model development

3.1. Model domain and assumptions

The model used in this work is based on the previously published work by the authors [37], in which a 1D physics-based cell model of VRFB in symmetric cell configuration was developed. In this work, the previously developed model [37] has been extended in order to simulate a VRFB during charge-discharge cycles. The charge-discharge reactions at positive and negative side are:

$$VO^{2+} + H_2O \rightleftharpoons^{charge}_{discharge} VO_2^+ + 2H^+ + e^- \ at\ (+) \tag{6}$$

$$V^{3+} + e^- \rightleftharpoons^{charge}_{discharge} V^{2+} \ at\ (-) \tag{7}$$

The model has been also integrated with the self-discharge reactions due to vanadium cross-over [17].

$$V^{2+} + 2VO_2^+ + 2H^+ \rightarrow 3VO^{2+} + H_2O \quad at\ (+) \tag{8}$$

$$V^{3+} + VO_2^+ \rightarrow 2VO^{2+} \quad at\ (+) \tag{9}$$

$$V^{2+} + VO^{2+} + 2H^+ \rightarrow 2V^{3+} + H_2O \quad at\ (-) \tag{10}$$

$$2V^{2+} + VO_2^+ + 4H^+ \rightarrow 3V^{3+} + 2H_2O \quad at\ (-) \tag{11}$$

The model domain is reported in Fig. 1 and the main model assumptions, as frequently reported in the literature, are:

- Isothermal domain at 298.15 K [18,19,38]
- Incompressible electrolytes [19,39,40]
- Fully mixed electrolytes [19,38,40]
- Isotropic mass and charge transfer properties of the membrane and the electrodes [19,40]
- Absence of oxygen evolution reaction (OER) and hydrogen evolution reaction (HER) [19,40]
- Diluted solution approximation [19,40]

In the following, just the main model governing equations for each component and the differences with respect to the previously published

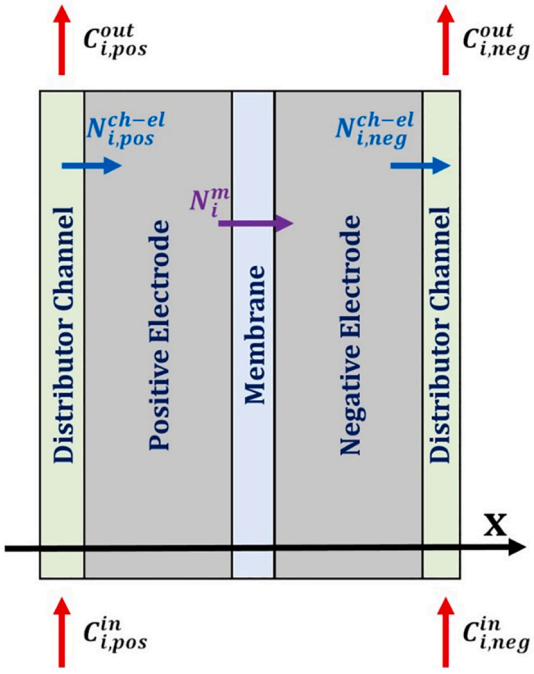

Fig. 1. Model domain (not to scale) [6].

model has been reported. More details about model development can be found in [37].

3.2. Negative electrode

The equations adopted in the negative electrode are the same of [37], with some differences given by the presence of the cross-contamination. The conservation of mass for each charged species is thus defined using the following eqs. [6]:

$$\nabla\cdot\overrightarrow{N_{V^{2+}}} = -i_{v,neg}/F - 2RR_{cx,1} - RR_{cx,2} - RR_{cx,4} \tag{12}$$

$$\nabla\cdot\overrightarrow{N_{V^{3+}}} = i_{v,neg}/F + 3RR_{cx,1} + 2RR_{cx,2} - RR_{cx,3} \tag{13}$$

$$\nabla\cdot\overrightarrow{N_{VO^{2+}}} = -2RR_{cx,2} + 2RR_{cx,3} + 3RR_{cx,4} \tag{14}$$

$$\nabla\cdot\overrightarrow{N_{VO_2^+}} = -RR_{cx,1} - RR_{cx,3} - 2RR_{cx,4} \tag{15}$$

$$\nabla\cdot\overrightarrow{N_{H^+}} = -4RR_{cx,1} - 2RR_{cx2} - 2RR_{cx,4} \tag{16}$$

Where $i_{v,neg}$ is the volumetric current density of the reaction of the redox couple V^{2+}/V^{3+} and it follows Butler-Volmer kinetic:

$$i_{v,neg} = aFK_{neg}\left(C^s_{V^{2+}} e^{\alpha_{neg}\frac{F}{RT}\eta_{neg}} - C^s_{V^{3+}} e^{(\alpha_{neg}-1)\frac{F}{RT}\eta_{neg}}\right) \tag{17}$$

Where a is the electrode specific area, α_{neg} is the negative charge transfer coefficient and C^s indicates the species concentration at the electrode surface.

The terms $RR_{cx,k}$ indicate the reaction rates of reactions Eq. (12)–(16), modelled according to the following power laws [6].

$$RR_{cx,1} = K_{cx,1}\left(C^b_{V^{2+}}/C_0\right)^2\left(C^b_{VO^{2+}}/C_0\right) \tag{18}$$

$$RR_{cx,2} = K_{cx,2}\left(C^b_{V^{2+}}/C_0\right)\left(C^b_{VO^{2+}}/C_0\right) \tag{19}$$

$$RR_{cx,3} = K_{cx,3}\left(C^b_{VO^{2+}}/C_0\right)\left(C^b_{V^{3+}}/C_0\right) \tag{20}$$

$$RR_{cx,4} = K_{cx,4}\left(C^b_{VO^{2+}}/C_0\right)^2\left(C^b_{V^{2+}}/C_0\right) \tag{21}$$

in which $K_{cx,k}$ is the kinetic constant of the k-cross-over reaction, C_0 is the reference concentration and C^b is the species concentration relative to the bulk electrolyte.

The charge conservation for the negative electrode results equal to:

$$\nabla\cdot\overrightarrow{i_l} = i_{v,neg} \tag{22}$$

Where i_l is the current density of the liquid phase.

3.3. Positive electrode

The governing equations for the positive electrode are the same of the negative one with some modifications due to the different reactions involved. The molar balance of the species V^{2+}, V^{3+}, VO^{2+}, VO_2^+ H^+ are defined by the following equations:

$$\nabla\cdot\overrightarrow{N_{V^{2+}}} = -2RR_{cx,1} - RR_{cx,2} - RR_{cx,4} \tag{23}$$

$$\nabla\cdot\overrightarrow{N_{V^{3+}}} = 3RR_{cx,1} + 2RR_{cx,2} - RR_{cx,3} \tag{24}$$

$$\nabla\cdot\overrightarrow{N_{VO^{2+}}} = -i_{v,pos}/F - 2RR_{cx,2} + 2RR_{cx,3} + 3RR_{cx,4} \tag{25}$$

$$\nabla\cdot\overrightarrow{N_{VO_2^+}} = i_{v,pos}/F - RR_{cx,1} - RR_{cx,3} - 2RR_{cx,4} \tag{26}$$

$$\nabla\cdot\overrightarrow{N_{H^+}} = 2i_{v,pos}/F - 4RR_{cx,1} - 2RR_{cx2} - 2RR_{cx,4} \tag{27}$$

Where $i_{v,pos}$ is the volumetric current density of the reaction of the redox couple VO^{2+}/VO_2^+ and it is computed via Butler-Volmer equation:

$$i_{v,pos} = aFK_{pos}\left(C^s_{VO^{2+}} e^{\alpha_{pos}\frac{F}{RT}\eta_{pos}} - C^s_{VO_2^+} e^{(\alpha_{pos}-1)\frac{F}{RT}\eta_{pos}}\right) \tag{28}$$

The same reaction rates adopted in the negative electrode are used. The charge conservation for the positive electrode is:

$$\nabla\cdot\overrightarrow{i_l} = i_{v,pos} \tag{29}$$

3.4. Membrane

Since no reactions take place in the membrane, the mass and the charge conservation result equal to:

$$\nabla\cdot\overrightarrow{N_i} = 0 \tag{30}$$

$$\nabla\cdot\overrightarrow{i_l} = 0 \tag{31}$$

The main difference with respect to [37] is the presence of the flux of every charged species in the membrane described by the Nernst-Planck equation:

$$N_i = -D_i^m\overrightarrow{\nabla C_i} - z_i\frac{F}{RT}D_i^m C_i\overrightarrow{\nabla\phi_{ionic}} \tag{32}$$

The membranes employed in this work are cation exchange membranes, thus the fluxes of negative charged ions are limited due to the presence of negatively charged sulphonic groups. Therefore, the fluxes of HSO_4^- and SO_4^{2-} are set to 0 [6].

For the determination of the liquid phase potential the same equation used in the electrodes is adopted:

$$\overrightarrow{\nabla\phi_{ionic}} = -\frac{RT}{F}\frac{\sum_i \frac{z_i\overrightarrow{N_i}}{D_i^m}}{\sum_i z_i^2 C_i^b} \tag{33}$$

3.5. Numerical resolution

The 1D VRFB model is implemented in MATLAB® and it is subjected

to the following boundary conditions. The continuity of fluxes of the charged species between the electrodes and the membrane is guaranteed for all the charged species:

$$N_i^{pos,R} = N_i^{mem,L}\ i = \left\{V^{2+}, V^{3+}, VO^{2+}, VO_2^+, H^+, HSO_4^-\right\} \tag{34}$$

$$N_i^{neg,L} = N_i^{mem,R}\ i = \left\{V^{2+}, V^{3+}, VO^{2+}, VO_2^+, H^+, HSO_4^-\right\} \tag{35}$$

Where *pos*, *neg* and *mem* stand for positive electrode, negative electrode and membrane, while *R* and *L* indicate the right or left boundary of the considered domain with respect to the scheme of Fig. 1.

The species concentration at the interfaces between the membrane and the electrodes is considered continuous for all the charged species:

$$C_i^{pos,R} = C_i^{mem,L}\ i = \left\{V^{2+}, V^{3+}, VO^{2+}, VO_2^+, H^+, HSO_4^-\right\} \tag{36}$$

$$C_i^{neg,L} = C_i^{mem,R}\ i = \left\{V^{2+}, V^{3+}, VO^{2+}, VO_2^+, H^+, HSO_4^-\right\} \tag{37}$$

The ionic current density at the membrane interfaces is set equal to the operating one, while is set to 0 at the channel-electrode interfaces:

$$i_l^{pos,L} = 0 \tag{38}$$

$$i_l^{mem,L} = i_{VRFB} \tag{39}$$

The ionic potential continuity is guaranteed at the membrane boundaries:

$$\phi_l^{pos,R} = \phi_l^{mem,L} \tag{40}$$

$$\phi_l^{mem,R} = \phi_l^{neg,L} \tag{41}$$

In addition, it is set to 0 at the right boundary of the negative electrode as a reference potential.

$$\phi_s^{neg,R} = 0 \tag{42}$$

The voltage of the battery is thus computed:

$$\Delta V = \phi_s^{pos,L} - \phi_s^{neg,R} \tag{43}$$

The species flux between the distributor channel and the electrode is computed following the approach proposed by Zago et al. [37]

$$N_i^{ch-el} = h_{ch,i}\left(C_i^{ch} - C_i^{ch-el}\right) \tag{44}$$

where $h_{ch,i}$ is the convective mass transport coefficient for the *i* species and C_i^{ch} is the bulk concentration in the channel, computed as an average between the inlet and the outlet concentration:

$$C_i^{ch} = \frac{C_i^{in} - C_i^{out}}{2} \tag{45}$$

C_i^{out} is obtained from a molar balance on the distributor channel:

$$C_i^{out} = \frac{N_i^{el-ch} A_{geo}}{\dot{Q}} \tag{46}$$

Where A_{geo} is the area of the electrode and $\dot{Q}$ is the volumetric flow rate.

By substituting Eqs. (45) and (46) in Eq. (44) and mathematically rearranging it is possible to obtain the boundary conditions for the electrode-channel interface for both the positive and the negative electrodes:

$$N_i^{pos,L} = \frac{h_{ch,i}}{1 + \frac{h_{ch,i} A_{geo}}{2\dot{Q}}}\left(C_i^{pos,in} - C_i^{pos,L}\right) \tag{47}$$

$$N_i^{neg,R} = \frac{h_{ch,i}}{1 + \frac{h_{ch,i} A_{geo}}{2\dot{Q}}}\left(C_i^{neg,R} - C_i^{neg,in}\right) \tag{48}$$

3.6. Simulation of cycling operation

The model is used to simulate charge-discharge cycles with fixed cut-off voltages. These are simulated with a succession of steady-state conditions solved with the equation previously described, taking as input the applied current density and the inlet concentrations at the time instant *t*, computed starting from the steady-state condition at time instant *t-1* as:

$$C_{i,t}^{pos,in} = C_{i,t-1}^{pos,in} - \frac{N_{i,t-1}^{pos,R} A_{geo}}{V_{sol}} \Delta t \tag{49}$$

$$C_{i,t}^{neg,in} = C_{i,t-1}^{neg,in} - \frac{N_{i,t-1}^{neg,L} A_{geo}}{V_{sol}} \Delta t \tag{50}$$

where Δt is the timestep of the simulation and V_{sol} is the volume of the electrolyte solution.The SoC of the positive and the negative electrolyte is computed as:

$$SoC_t^{pos} = \frac{C_{VO_2^+,t}}{C_{VO_2^+,t} + C_{VO^{2+},t}} \tag{51}$$

$$SoC_t^{neg} = \frac{C_{V^{2+},t}}{C_{V^{2+},t} + C_{V^{3+},t}} \tag{52}$$

The total capacity of the electrolyte is determined by the amount of vanadium ions present in the solution, and it is determined as:

$$Cap_{tot,t}^{pos} = Cap_{tot,t-1}^{pos} + \left(\left|N_{V^{2+}}^m\right| + \left|N_{V^{3+}}^m\right| - \left|N_{VO^{2+}}^m\right| - \left|N_{VO_2^+}^m\right|\right) FA_{geo}\Delta t \tag{53}$$

$$Cap_{tot,t}^{neg} = Cap_{tot,t-1}^{neg} + \left(-\left|N_{V^{2+}}^m\right| - \left|N_{V^{3+}}^m\right| + \left|N_{VO^{2+}}^m\right| + \left|N_{VO_2^+}^m\right|\right) FA_{geo}\Delta t \tag{54}$$

Where N_i^m is the flux of the *i* species across the membrane. The capacity of the positive and negative electrolytes is dependent on the state of charge and is calculated as:

$$Cap_t^{pos} = Cap_{tot,t}^{pos}\ SoC_t^{pos} \tag{55}$$

$$Cap_t^{neg} = Cap_{tot,t}^{neg}\ SoC_t^{neg} \tag{56}$$

This quantity is determined by the amount of the charged species in the positive and negative side. It is possible to compute it as:

$$Cap_t^{pos} = Cap_{t-1}^{pos}\left(i_{VRFB}/F - \left|N_{VO_2^+}^m\right| - 2\left|N_{V^{2+}}^m\right| - \left|N_{V^{3+}}^m\right|\right) FA_{geo}\Delta t \tag{57}$$

$$Cap_t^{neg} = Cap_{t-1}^{neg}\left(i_{VRFB}/F - \left|N_{V^{2+}}^m\right| - \left|N_{VO^{2+}}^m\right| - 2\left|N_{VO_2^+}^m\right|\right) FA_{geo}\Delta t \tag{58}$$

Where the term $\frac{i_{VRFB}}{F}$ takes into account the contribute of the operating current of the battery, while the other terms consider the effects of the crossover fluxes, that always lead to a reduction of battery capacity. The simulation of charge and discharge operations lasts until the cut-off limit is reached, fixed at 1.65 V and 1 V, respectively.

4. Results and discussions

4.1. Commercial electrolyte

4.1.1. Experimental results

This paragraph reports the results of charge-discharge cycles for the three different membranes using the commercial electrolyte. Fig. 2A illustrates the evolution of the discharged capacity during the 13 days of operation.

It is worth noting that E98–05, E87–05 and E98–09 show a similar and severe capacity decay during the first 3 days of operation, despite a different thickness and equivalent weight. Then, the discharged capacity tends to a stable value for E98–05 and E98–09, while it continuously decreases with a linear trend for the E87–05.

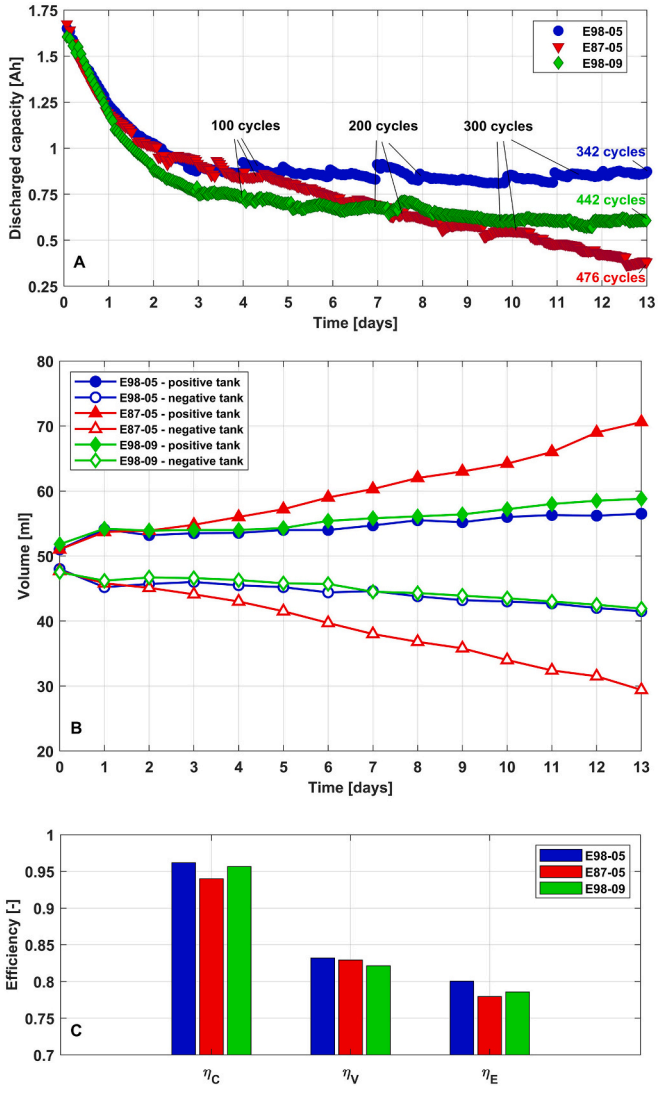

Fig. 2. Charge-discharge cycles with E98–05, E87–05 and E98–09 using commercial electrolyte: A) discharged capacity; B) electrolytes volume variation; C) mean efficiencies.

In the investigated operating conditions, no side reactions are expected to occur due to the limited value of upper potential limit and therefore the coulombic efficiency can be directly correlated with the intensity of crossover phenomena, as stated in [41]. Fig. 2C reports the average values of battery efficiencies during charge-discharge cycles. E98–05 and E98–09 exhibit similar CE values, equal to 96.2% and 95.7%, respectively. This result suggests that vanadium ions cross-over is not only regulated by diffusion mechanism, which is hindered adopting thicker membranes. Instead E87–05 is characterized by a lower CE, equal to 94%. These results are coherent with [21], in which it is reported that higher equivalent weight leads to a reduction of ion crossover phenomena. Moreover, this is in agreement with the measured capacity decay of Fig. 2A, in which E87–05 presents a greater capacity loss. The mean voltage efficiency values are similar among the different membranes: E98–09 presents a slightly lower value most probably associated to the higher membrane thickness, resulting in increased ohmic losses. Coherently with similar voltage efficiency among the different membranes, energy efficiencies resemble the trend of coulombic efficiencies.

Fig. 2B reports the electrolytes volume variation. It can be noticed that neither the positive and the negative electrolyte volume starts exactly from 50 ml at day 0: this is due to the volume variation occurring during the electrolyte preparation, when 50 ml of $V^{3.5+}$ is oxidized to V^{4+} at positive electrode and reduced to V^{3+} at negative electrode. Anyway, for all the three membranes this initial volume variation occurring before charge-discharge cycles is limited. In the first day of operation the same volume variation takes place regardless the adopted membrane: positive electrolyte increases by 2 ml, while the negative one decreases by 2 ml. Then, once again, E98–05 and E98–09 show a similar trend: the volume remains constant until day 4 and subsequently it varies linearly (about 0.5 ml day^{-1}) at both sides until the end of the test. The final volume is about 58 ml for the positive electrolyte and 42 ml for the negative one. Instead E87–05 exhibits a higher (about 1.6 ml day^{-1}) and a continuous volume variation starting at day 1. The final volume is 71 ml and 29 ml for the positive and negative electrolyte, respectively.

Appendix A reports a comparison between battery performance with commercial electrolyte prepared according to the procedure described in Section 2.2 and a commercial electrolyte from GfE chemicals [30]. The reported trends are analogous, confirming that the obtained results are not related to the methodology used to prepare the commercial electrolyte.

The analysis of charge-discharge cycles adopting the commercial electrolyte highlights a consistency between the evolution of capacity and the trend of volume variation: higher capacity decay is generally associated with a greater volume variation. Moreover, regardless of thickness and equivalent weight all the membranes evidence a similar and strong initial capacity decay, whose origin is not completely understood. In order to get an insight into the initial capacity decay, a model-based analysis of the first charge-discharge cycles is provided in the next paragraph.

4.1.2. *Model based analysis of the initial capacity decay*

The developed model considers all the main physical phenomena regulating battery operation and vanadium cross-over. The aim of the present model-based analysis is not to quantitatively reproduce the experimental data, but to understand the origin of the initial capacity decay and therefore conceive a mitigation strategy, that will be validated experimentally in the next sections. In order to perform a rigorous model experimental validation and thus improve the capability of the model to quantitatively simulate the capacity decay, it would be necessary to reproduce with high accuracy species concentration and ionic potential at the membrane interfaces. These quantities are not uniform across cell area and are strongly influenced by current distribution and local electrolyte velocities inside the porous electrode [42]. The detailed simulation of the above mentioned quantities can be implemented only with the aid of computational fluid dynamics (CFD) model in a 3D domain, resulting in a dramatic increase of computational time, especially for the simulation of several cycles. Therefore the adoption of a more complex model and the rigorous experimental validation are out of the scope of this work.

The values of the adopted model parameters are reported in Table 1.

Fig. 3 reports the simulations of the first 15 charge-discharge cycles using the commercial electrolyte.

The discharged capacity (Fig. 3A) sharply decreases from 1.25 Ah to 0.78 Ah during the first 7 cycles and then it tends to stabilize around 0.75 Ah. Therefore, the developed model qualitatively reproduces the initial capacity decay. The faster dynamic of capacity decay predicted by the model can be reduced with an extensive experimental calibration, but this is out of the scope of the work.

Fig. 3B illustrates the evolution of vanadium ions cross-over fluxes through the membrane: accordingly with the model domain of Fig. 1, fluxes directed from positive to negative electrode are positive, while fluxes directed from negative to positive electrode are negative. It is worth noting that the first 7 cycles, in which the most of the capacity drop occurs, are characterized by higher values of V^{2+} and V^{3+} fluxes towards positive electrode and reduced values of V^{4+} and V^{5+} fluxes towards negative electrode. This leads to a net displacement of

Table 1
Adopted model parameters.

Parameter		Value
Temperature	T	298 K
Cell Area	A_{geo}	$25x10^{-4}$ m^2
Specific Area	a	$9.76x10^{4}$ m^{-1}
Electrode Thickness	l_{el}	$2x10^{-3}$ m
Pores radius	r_p [19]	$50.3x10^{-6}$ m
Electrode porosity	ϵ [40]	0.93
Electrode electric conductivity	σ_s [19]	66.7 $s\,m^{-1}$
Formal equilibrium Potential V^{2+}/V^{3+}	E_0^{neg} [6]	-0.332 V
Formal equilibrium Potential VO^{2+}/VO_2^+	E_0^{pos} [6]	1.121 V
Negative Charge Transfer Coefficient	α_{neg} [6]	0.5
Positive Charge Transfer Coefficient	α_{pos} [6]	0.5
Negative Kinetic Constant	K_{neg}	$6.69x10^{-7}$ $m\,s^{-1}$
Positive Kinetic Constant	K_{pos}	$1.76x10^{-5}$ $m^2\,s^{-1}$
Electrolyte Diffusivity V^{2+}	$D^{el}_{V^{2+}}$	$4x10^{-9}$ $m^2\,s^{-1}$
Electrolyte Diffusivity V^{3+}	$D^{el}_{V^{3+}}$	$4x10^{-9}$ $m^2\,s^{-1}$
Electrolyte Diffusivity VO^{2+}	$D^{el}_{VO^{2+}}$	$4x10^{-9}$ $m^2\,s^{-1}$
Electrolyte Diffusivity VO_2^+	$D^{el}_{VO_2^+}$	$4x10^{-9}$ $m^2\,s^{-1}$
Electrolyte Diffusivity H^+	$D^{el}_{H^+}$	$8x10^{-7}$ $m^2\,s^{-1}$
Electrolyte Diffusivity HSO_4^-	$D^{el}_{HSO_4^-}$ [19]	$1.33x10^{-9}$ $m^2\,s^{-1}$
Electrolyte Diffusivity SO_4^{2-}	$D^{el}_{SO_4^{2-}}$ [19]	$1.33x10^{-9}$ $m^2\,s^{-1}$
Cross-over Reaction Rate Constant	$K_{cx,k}$ [6]	$1x10^{6}$ $mol\,m^{-3}\,s^{-1}$
Membrane Thickness	l_m	$50x10^{-6}$ m
Membrane Diffusivity V^{2+}	$D^{m}_{V^{2+}}$ [19]	$3.125x10^{-12}$ $m^2\,s^{-1}$
Membrane Diffusivity V^{3+}	$D^{m}_{V^{3+}}$ [19]	$3.125x10^{-12}$ $m^2\,s^{-1}$
Membrane Diffusivity VO^{2+}	$D^{m}_{VO^{2+}}$ [19]	$5x10^{-12}$ $m^2\,s^{-1}$
Membrane Diffusivity VO_2^+	$D^{m}_{VO_2^+}$ [19]	$1.17x10^{-12}$ $m^2\,s^{-1}$
Membrane Diffusivity H^+	$D^{m}_{H^+}$ [19]	$3.35x10^{-9}$ $m^2\,s^{-1}$

vanadium ions from negative to positive side, resulting in a reduction of the discharged capacity.

The reason of such a behavior can be understood analysing the Nernst-Planck equation (Eq. (32), that regulates the ions fluxes through the separator. The flux of a generic charged species is due to two transport mechanisms: diffusion by concentration gradient and migration by ionic potential gradient. Fig. 3C reports the evolution of the mean ionic potential gradient across the membrane. According to Eq. (32) and the convention of Fig. 1, in the first cycles the high and positive value of the ionic potential gradient across the membrane enhances the fluxes of V^{2+} and V^{3+} towards the positive electrode (negative values in Fig. 3B) and hinders the fluxes of V^{4+} and V^{5+} towards the negative electrode (positive values in Fig. 3B).

As reported in Zago et al. [37], the ionic potential is considerably affected by proton concentration. Analysing the value of the mean proton concentration gradient across the membrane (Fig. 3D) it can be noticed that at cycle 0 it is negative. In fact during the pre-charge phase, when $V^{3.5+}$ is oxidized to V^{4+} at positive side and reduced to V^{3+} at negative side, protons are produced at positive electrode and consumed at negative one, following the reactions reported in Eq. (6) and Eq. (7), respectively. This leads to a higher concentration of H^+ at positive side tank with respect to the negative one, that results in a negative proton concentration gradient across the membrane according to the convention of Fig. 1. Considering the reactions occurring at positive electrode during nominal battery operation (Eq. (6)), protons are produced during charge and consumed during discharge. This leads to an increasing proton concentration gradient during the charge phase and a consequent decreasing trend during the discharge phase, as reported in Fig. 3D during the first cycle. After the first cycles, the proton concentration gradient tends to stabilize due to a different intensity and direction of migrative and diffusive proton fluxes during charge and discharge phases and then it oscillates around 0. From model simulations it can be clearly noticed that in the first cycles, when the initial capacity drop occurs, the value of ∇C_{H^+} is always negative.

The relation between a negative value of ∇C_{H^+} and a positive $\nabla \phi_{ionic}$

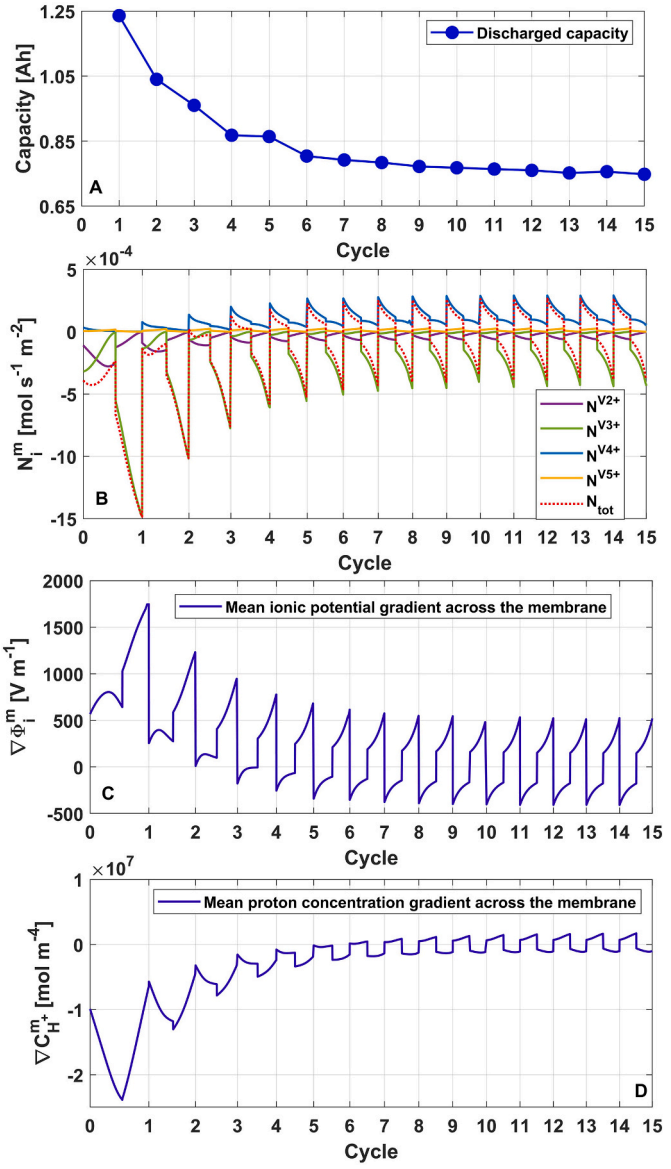

Fig. 3. Simulation results during the first 15 cycles: A) discharged capacity; B) vanadium cross-over fluxes; C) mean ionic potential gradient across the membrane; D) mean proton concentration gradient across the membrane.

can be explained analysing simultaneously the Nernst-Planck equation for H^+ in Eq. (59) and the charge conservation through the membrane in Eq. (60), in which the contribution of H^+ has been made explicit:

$$N_{H^+} = -D_{H^+}\nabla C_{H^+} - z_{H^+}\frac{F}{RT}D_{H^+}C_{H^+}\nabla\phi_{ionic} \tag{59}$$

$$i_l = \sum_i z_i N_i F = z_{H+}N_{H+}F + \sum_{i=2:5} z_{Vi}N_{Vi}F \tag{60}$$

In VRFB employing a cation exchange membrane, proton flux represents the main contribution to the ionic current due to the higher diffusivity of H^+ with respect to the other positively charged ions [6,19,39,43–49]. During charge i_l is directed from positive to negative electrode (i.e., it is positive). In the first cycles, when ∇C_{H^+} is strongly negative as previously explained, the contribution of diffusive term to the proton flux N_{H^+} consequently assumes a strongly positive value. Since charge conservation through the membrane must be respected (Eq. (60)) $\nabla\phi_{ionic}$ assumes a positive value, leading to a negative contribution of migration to the proton flux in Eq. (62). Conversely,

during discharge, the ionic current is directed from negative to positive electrode (i.e., it is negative). Again, when ∇C_{H^+} is strongly negative, the diffusive term of N_{H^+} assumes a strongly positive value and in order to guarantee a sufficient flux of protons towards the positive side, $\nabla\phi_{ionic}$ assumes a positive value leading to a negative contribution of migration to the proton flux (59).

It follows that as long as a negative ∇C_{H^+} is present across the membrane, the resulting positive value of $\nabla\phi_{ionic}$ in charge and discharge enhances the flux of V^{2+} and V^{3+} towards the positive electrode and hinders the flux of V^{4+} and V^{5+} towards the negative electrode, as already reported in Fig. 3B. This causes a net displacement of vanadium ions from negative to positive side, leading to the sharp capacity decay observed in the first charge-discharge cycles.

The presented modelling analysis of the first charge-discharge cycles evidences the importance of ionic potential gradient though the membrane and the complex interaction among the fluxes of positively charged ions in order to guarantee the imposed ionic current. It emerges that diffusion is not the main transport mechanism, since the contribution of migration is strongly increases in the first cycles. This is in agreement with the similar capacity decay observed in Fig. 2A for membranes with different thickness (E98–05 and E98–09).

Moreover, the developed model permits to analyse the effects of electrolyte composition on ionic fluxes through the membrane. In fact, referring to the contribution of migration to the proton flux in Eq. (*59* and considering that proton flux represents the main contribution to the ionic current, fixing the ionic current it can be clearly noticed that an increased proton concentration C_{H^+} leads to a lower ionic potential gradient. As a consequence, the contribution of migration to vanadium cross-over is reduced and therefore also the initial capacity decay.

Considering the effects of proton concentration and proton concentration gradient through the membrane, the model has been used to simulate VRFB operation during the first cycles adopting different electrolyte compositions. In particular, two different electrolyte compositions[2] have been simulated: the first one in which proton concentration between the two electrolyte tanks has been set to 0 at the beginning of cycling operation (referred as equal proton concentration), the second one characterized by an increased proton concentration with respect to the commercial electrolyte (referred as increased proton concentration). Fig. 4A illustrates the evolution of the ionic potential gradient across the membrane during the first charge-discharge cycles, while the corresponding net vanadium cross-over is reported in Fig. 4B.

As can be noticed, with the equal proton concentration electrolyte the ionic potential gradient always oscillates around zero and consequently the net vanadium crossover from negative to positive electrode is limited. Considering the increased proton concentration electrolyte, as expected, a lower ionic potential gradient is developed and the net vanadium flux from negative to positive electrode is once again strongly reduced.

In the next sections, the effect of the different electrolyte compositions predicted by model simulations is verified experimentally. The experimental analysis of the different electrolyte compositions is initially performed adopting E98–05 as membrane and then it is extended to all the three membranes tested.

4.2. Electrolyte with equal proton concentration

4.2.1. Electrolyte preparation

The electrolyte characterized by an equal proton concentration between the two tanks at the beginning of the cycling test is obtained by employing at positive and negative side two electrolyte solutions with different initial acid molarity before the beginning of charge-discharge cycles. In particular, the acid molarity at positive side is kept at 2 M,

[2] The details about electrolyte with equal proton concentration and increased proton concentration are provided in Section 4.2.1 and 4.3.1, respectively.

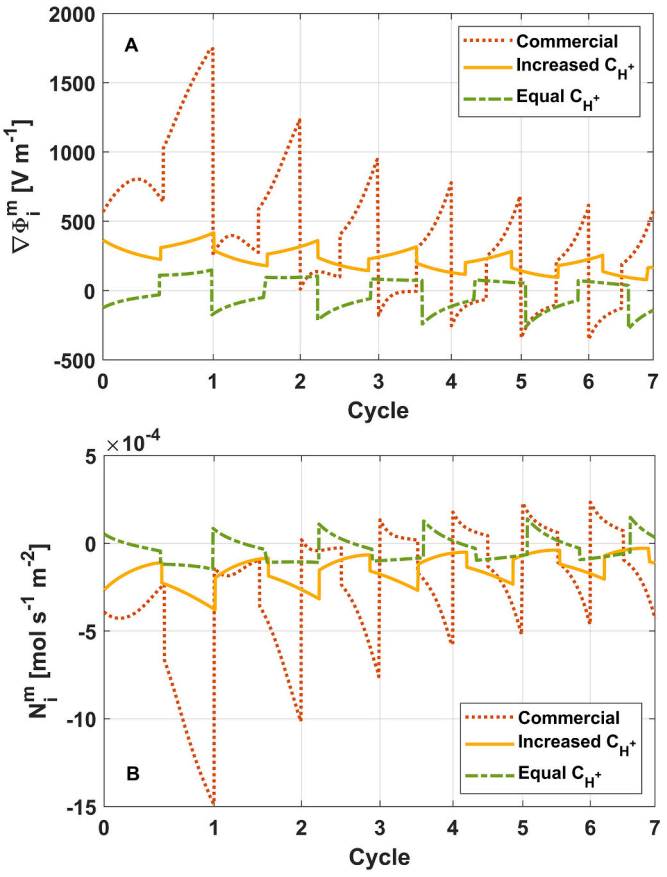

Fig. 4. Simulation results during the first 7 cycles using different electrolytes: A) mean ionic potential gradient across the membrane; B) net vanadium cross-over through the membrane.

as for the preparation of commercial electrolyte. Instead at the negative side the electrolyte molarity is increased to 3.5 M: this value is evaluated with the developed model.

The experimental procedure for the preparation of this electrolyte is similar to the one adopted for commercial one. Three reservoirs with 65[1] ml of electrolyte are prepared: one tank with 1.6 M $VOSO_4$ dissolved in a 2 M aqueous solution of sulfuric acid and two tanks with 1.6 M of $VOSO_4$ dissolved in a 3.5 M aqueous solution of sulfuric acid. These two reservoirs are subjected to the pre-charge phase, where V^{4+} is oxidized to V^{5+} at positive electrode and reduced to V^{3+} at the negative one. Then, the tank containing V^{5+} at positive side is replaced with the one with V^{4+} in 2 M sulfuric acid. Finally, before charge-discharge cycles, both battery tanks are filled with 50 ml of electrolyte.

4.2.2. Experimental results

Fig. 5A reports the comparison of discharged capacity during 13 days of operation between the electrolyte with equal proton concentration and the commercial one.

It can be clearly noticed that the adoption of equal proton concentration electrolyte permits to eliminate the initial and sharp capacity decay observed with the commercial one. The discharged capacity decreases linearly from the beginning to the end of the test, approaching the value of 1.15 Ah at day 13. The higher discharged capacity is related to a lower net vanadium cross-over, that affects also battery efficiencies, reported in Fig. 5C. The adoption of equal proton concentration electrolyte presents slightly higher mean coulombic efficiency, while the increase of mean voltage efficiency is more evident. The resulting mean energy efficiency is nearly 5% higher compared to the case of commercial electrolyte, highlighting the strong impact of electrolyte

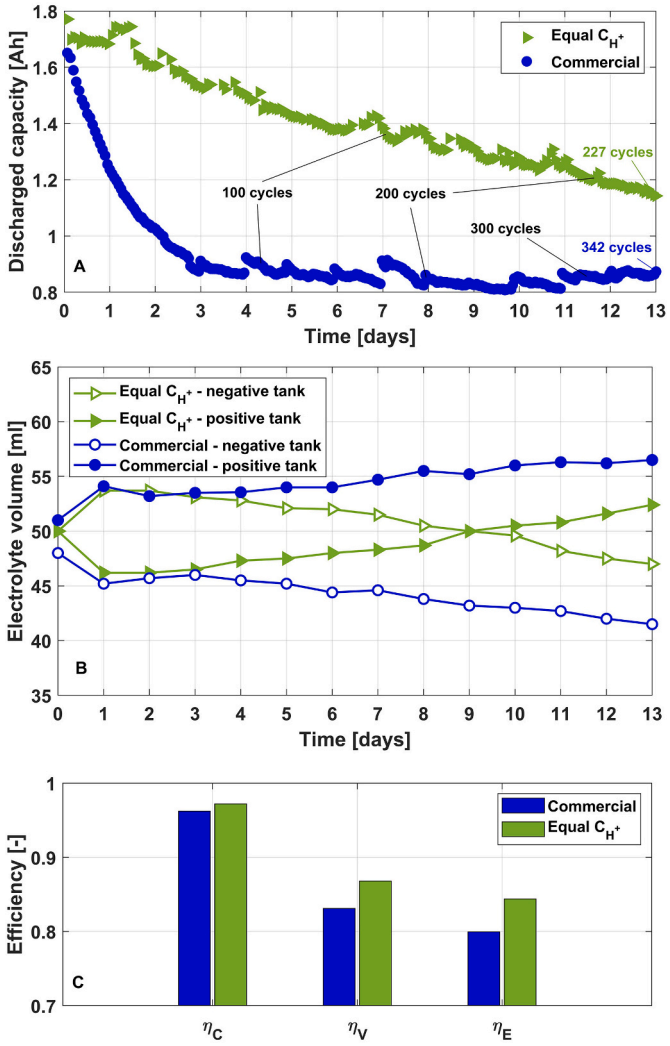

Fig. 5. Charge-discharge cycles with E98–05 using electrolyte with equal proton concentration: A) discharged capacity; B) electrolyte volume variation; C) mean efficiencies.

composition on battery performance.

The volume variation occurring with equal proton concentration electrolyte is reported in Fig. 5B: at day 1 the volume shows a 4 ml increase at negative side and a decrease by the same quantity at positive side. Instead from day 2 to the end of the test the positive side exhibits a linear increase of volume of about 0.5 ml day^{-1}, and the negative side shows a linear decrease at the same rate.

This test confirms model predictions and demonstrates that the reduction of proton concentration gradient across the membrane permits to eliminate the initial capacity decay and increases battery efficiencies. However, volume variation at day 1 adopting equal proton concentration electrolyte shows an opposite behavior compared to the commercial one. This aspect needs to be further analysed in order to properly modify and improve electrolyte preparation.

4.2.3. Analysis of the initial volume variation

All the performed tests highlighted a net volume variation in the first day of operation. As can be seen in Fig. 2B, this is not influenced by the adopted separator, while electrolyte composition plays a more relevant role. In fact, as reported in Fig. 5B, an opposite behavior at day 1 is noticed comparing commercial electrolyte and the one with equal proton concentration. Analysing in more details the evolution of volume reported in *Appendix B*, it can be noticed that the initial volume variation does not take place in one day, but it mainly occurs during the first charge-discharge cycle.

As reported in the introduction, volume variation is strictly related to water transport though the membrane, that is regulated by three different transport mechanisms: electro-osmotic drag, osmosis and water transported along with cross-over of vanadium ions. Moreover, water is produced and consumed at positive electrode during nominal battery operation and also the reactions associated to vanadium cross-over imply water production [20]: this further complicates the analysis of water transport in VRFB. However, a detailed analysis of water transport is out of the scope of this work.

Considering the abovementioned transport mechanisms and the very fast dynamic of the initial volume variation, it is reasonable to assume osmosis as the main cause of such volume variation. Osmosis is driven by the osmotic pressure difference across a semipermeable membrane [50], that is defined as:

$$\Delta P_{osm} = \frac{RT}{v_{H_2O}} ln\left(x_{pos}/x_{neg}\right) \tag{61}$$

where v_{H_2O} is the specific molar volume of water, x is the water molar fraction and *pos* and *neg* subscripts stands for *positive* and *negative* electrolyte, respectively. The corresponding water flux can be computed with Darcy's Law, as reported in [51]:

$$N_{H_2O,osm} = \frac{k_{mem}\,\rho}{\mu_{el} \cdot MM_{H_2O} \cdot th_{mem}} \cdot \Delta P_{osm} \tag{62}$$

where k_{mem} is the water permeability of the membrane, μ_{el} is the viscosity of the electrolyte, th_{mem} is the thickness of the membrane and MM_{H2O} is the molar mass of water. Coherently with the convention used in this work and the definition of the ΔP_{osm}, the osmosis water flux is positive when directed from positive to negative electrode (i.e., when x_{pos} is higher than x_{neg}).

The model developed in this work is thus used to compute the value of the initial water molar fraction at positive and negative side, calculated as the ratio between the number of water molecules and the total number of moles in the electrolyte:

$$x = \frac{mol_{H_2O}}{\sum^{species} mol_i} \tag{63}$$

The resulting water molar fractions and osmotic pressure gradient for the commercial electrolyte and the one with equal proton concentration are computed with the model and are reported in Table 2.

The initial osmotic pressure difference adopting commercial electrolyte is negative, leading to an osmotic water flux directed towards the positive side. Conversely, the equal proton concentration electrolyte has a positive initial osmotic pressure difference, that results in a water flux directed towards the negative side. This simplified modelling analysis is coherent with the initial volume variation observed in the experiments (Fig. 5B): commercial electrolyte exhibits a volume increase at the positive side, while the equal proton concentration one presents the opposite trend.

In order to confirm experimentally the osmotic nature of the initial volume variation, fixing at 2 M the acid molarity at positive side, the model is used to evaluate the acid molarity at negative side that ensures the same water molar fraction in the two tanks at the beginning of the test. The resulting value is 2.6 M. Fig. 6 reports the volume variation adopting the commercial electrolyte and the one modified in order to

Table 2
Initial water molar fractions and osmosis pressure difference between positive and negative electrolytes.

Electrolyte	x_{pos}	x_{neg}	ΔP_{osm} [bar]
Commercial	90.01%	91.26%	−19.0
Equal proton concentration	90.01%	87.46%	39.6

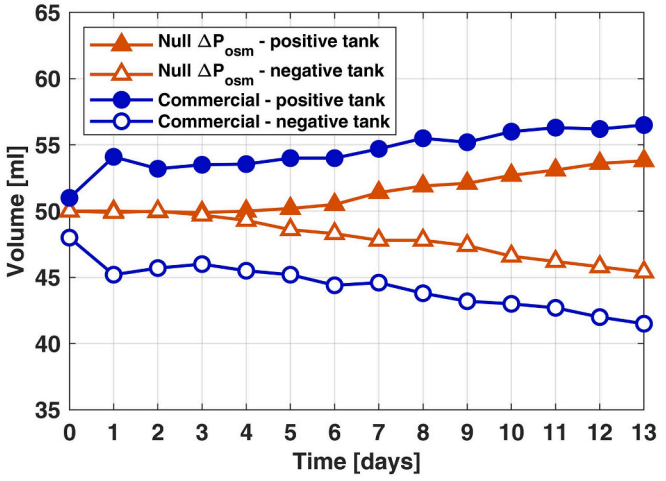

Fig. 6. Electrolytes volume variation during charge-discharge cycles with E98–05 using commercial electrolyte and electrolyte with null osmotic pressure difference.

minimize the osmotic pressure gradient across the membrane (referred as null osmotic pressure difference).

According to model predictions, the null osmotic pressure difference electrolyte is prepared using 1.6 M $VOSO_4$ in 2 M H_2SO_4 at positive side and 1.6 M $VOSO_4$ in 2.6 M H_2SO_4 at negative side. The preparation of the null osmotic pressure difference electrolyte is identical to the one described in Section 4.2.1, with the difference that the two tanks that undergo the pre-charge phase have an acid molarity of 2.6 M instead of 3.5 M. The volume variation of Fig. 6 evidences that the null osmotic pressure difference electrolyte eliminates the initial volume variation. Volume variation is null until day 3, while from day 4 it starts to linearly increase at positive side and decrease at negative side, with a rate similar to the one of commercial electrolyte.

The cause of the initial volume variation has been thus identified in the presence of an osmotic pressure difference across the membrane and it has been completely mitigated by using at negative side an electrolyte with higher acid molarity. The elimination of the initial osmotic pressure difference is combined in Section 4.4 with an electrolyte characterized by an increased proton concentration, whose effects are described in the following section.

4.3. Electrolyte with increased proton concentration

4.3.1. Electrolyte preparation

The electrolyte characterized by high proton concentration is obtained with the same procedure described in Section 2.2, with the difference that 1.6 M $VOSO_4$ is dissolved in an aqueous solution of sulfuric acid 4 M [52], instead of 2 M.

4.3.2. Experimental results

Fig. 7A reports the comparison of discharged capacity during 13 days of operation between the electrolyte with increased proton concentration and the commercial one.

It can be clearly noticed that the adoption of increased proton concentration electrolyte permits to eliminate the sharp initial capacity decay. Adopting the increased proton concentration electrolyte, the capacity exhibits a linear decreasing trend: after 13 days of operation the battery presents nearly the same capacity obtained with the commercial electrolyte just after 2 days of operation. As predicted by modelling analysis, the higher discharged capacity is related to a lower net vanadium cross-over, that affects also battery efficiencies. As reported in Fig. 7C, the adoption of increased proton concentration electrolyte presents higher mean coulombic and voltage efficiencies. The resulting

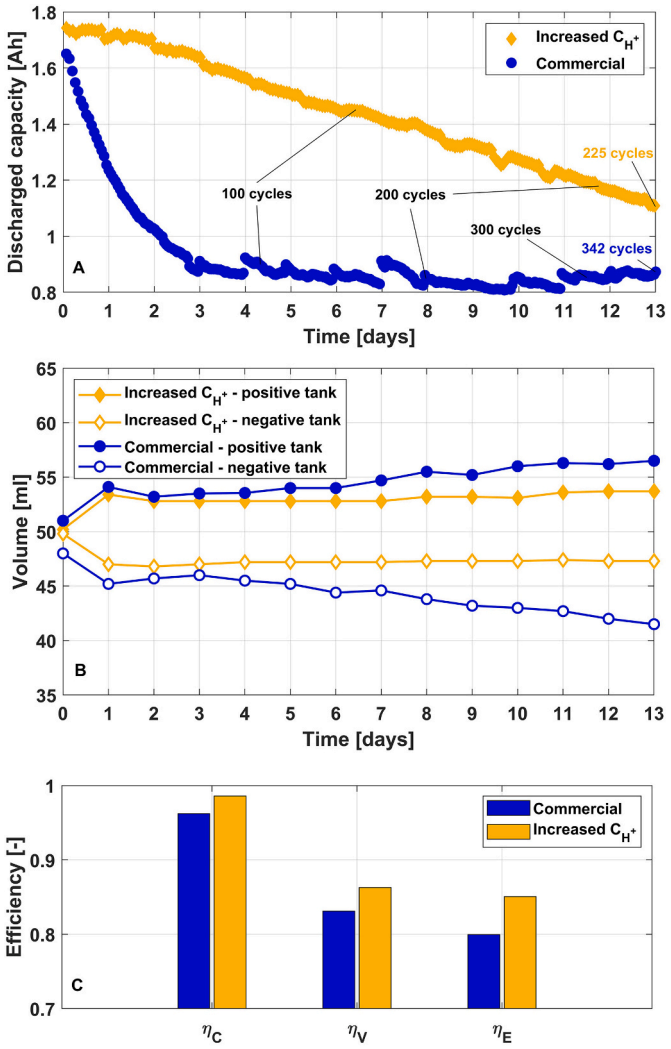

Fig. 7. Charge-discharge cycles with E98–05 using electrolyte with increased proton concentration: A) discharged capacity; B) electrolyte volume variation; C) mean efficiencies.

mean energy efficiency is nearly 5% higher compared to the case of commercial electrolyte, highlighting the strong impact of electrolyte composition on overall battery performance.

The evolution of electrolytes volume adopting increased proton concentration electrolyte is illustrated in Fig. 7B. The initial volume variation is analogous to the one observed with commercial electrolyte: positive electrolyte exhibits 3 ml volume increase, while the opposite occurs for the negative electrolyte. This is coherent with the similar preparation procedure, as described in Section 4.3.1, that causes the establishment of a negative osmotic pressure gradient leading to a water displacement from negative to positive side, as explained in section 0. Anyway, it is worth noting that the initial volume variation is more limited than the case of commercial electrolyte. Assuming that osmosis is the main water transport mechanism, this behavior is given by the higher ions concentration of both positive and negative electrolyte, that results in a lower water transport compared to the case of commercial electrolyte (the numerical calculation is reported in Appendix C).

Moreover, differently from the other tests performed, with increased proton concentration electrolyte no relevant volume variations are observed after the initial one. This behavior can be related to the combined effect of a lower cross-over with respect to the case of commercial electrolyte and a generally lower water transport resulting from the higher ions concentration of the electrolyte. In fact, the lower crossover

leads to more limited variation of the osmotic pressure gradient, that is rebalanced with a smaller water transport between the two electrolytes.

This test demonstrated the effectiveness in the reduction of the initial capacity drop also adopting increased proton concentration electrolyte. In addition, due to the higher ions concentration of the electrolyte, this solution leads to negligible volume variation after the initial one. In the next section, the electrolytes are prepared combining the effect of higher proton concentration and null osmotic pressure gradient, in order to maintain a negligible volume variation during the test while eliminating the initial one.

4.4. Electrolyte with null osmotic pressure difference and increased proton concentration

The final objective of this work is to mitigate both the capacity decay and the volume variation. This is obtained by adopting electrolytes characterized by high acid molarity, with a higher value at negative side in order to reduce the initial osmotic pressure difference across the membrane.

4.4.1. Electrolyte preparation

The acid molarity of negative electrolyte is set to 4.1 M: this upper limit is imposed by solubility issues [52]. Instead, the acid molarity of the positive electrolyte necessary to avoid the initial ΔP_{osm} between the two tanks is calculated with the model. The resulting value is 3.3 M. Therefore, 1.6 M $VOSO_4$ in 3.3 M H_2SO_4 is the composition adopted at positive side, while 1.6 M $VOSO_4$ in 4.1 M H_2SO_4 is the one used at negative side. The procedure for electrolytes preparation follows the same steps of the one described in Section 4.2.1, with the difference that 4.1 M is the acid molarity of the two tanks that undergo the pre-charge phase, while 3.3 M is the acid concentration of the electrolyte used at the positive side after the pre-charge phase.

4.4.2. Experimental results

Fig. 8A reports the evolution of discharged capacity using the electrolyte with null osmotic pressure difference and increased proton concentration. The discharged capacity decreases linearly from the beginning to the end of the test, approaching the value of 1.32 Ah at day 13. This value is higher with respect to the cases of equal proton concentration electrolyte (Fig. 5A) and increased proton concentration electrolyte (Fig. 7A), highlighting the effectiveness of the proposed electrolyte preparation.

Also the coulombic efficiency is the highest obtained and the mean value is equal to 98.9%, (Fig. 8C). The reasons of high discharge capacity and coulombic efficiency are related to the increase of proton concentration in the electrolytes and the reduction of proton concentration gradient across the membrane, obtained by increasing the acid molarity of negative side with respect to the one at positive side.

Moreover, with the null osmotic pressure difference and increased proton concentration electrolyte no volume variation occurs during the test (Fig. 8B). The absence of the initial volume variation is related to the null initial ΔP_{osm} between the two tanks, as already experienced in Section 4.2.3. Instead, the absence of the progressive volume variation after the first cycle is caused by the combined effect of reduced crossover fluxes and limited water transport experienced when increasing the ions concentrations of the electrolytes, as already explained in Section 4.3.2.

The electrolyte combining null osmotic pressure difference and increased proton concentration permitted to obtain a significant reduction of capacity decay and a complete mitigation of volume variation, evidencing the importance of electrolyte composition on battery performance.

This electrolyte preparation has been also applied to batteries employing E98–09 and E87–05 as membrane. The corresponding results are reported in *Appendix D*. Also with membranes with different thickness or equivalent weight the electrolyte with null osmotic pressure gradient and increased proton concentration is able to considerably improve battery performance, extending the validity of the proposed methodology for electrolyte preparation.

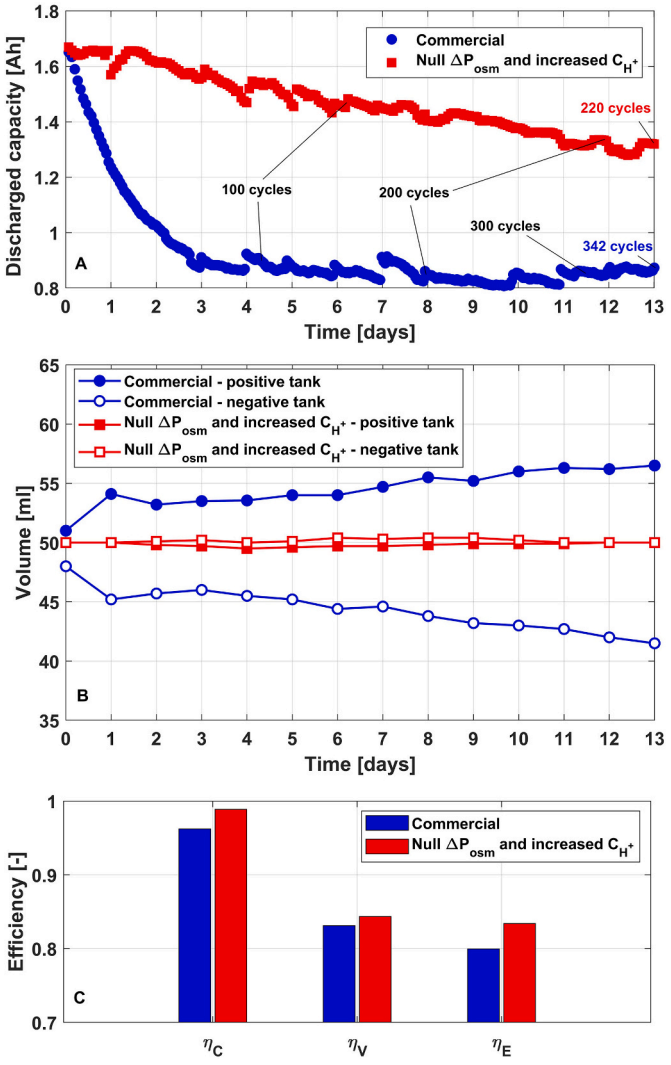

Fig. 8. Charge-discharge cycles with E98–05 using electrolytes with null osmotic pressure difference and increased proton concentration: A) discharged capacity; B) electrolyte volume variation; C) mean efficiencies.

5. Conclusions

In this work, the evolution of discharged capacity and electrolyte volume variation were firstly investigated adopting commercial electrolyte for hundreds of charge-discharge cycles in VRFBs employing different membranes, varying thickness and equivalent weight. Subsequently, with the support of a 1D physics-based model, the origin of the main phenomena regulating battery capacity decay and volume variation has been identified and different modifications in the preparation of electrolytes have been proposed in order to mitigate the above-mentioned operating issues.

The main conclusions of the work are the following:

- In the investigated operating conditions, regardless of the employed membrane, the adoption of commercial electrolyte implies a sharp initial capacity decay and electrolytes volume variation, with a strong variation in the first days of operation.
- The model-based analysis evidenced that the initial capacity decay adopting commercial electrolytes is related to the increased contribution of migration to vanadium cross-over, induced by proton concentration gradients across the membrane. Instead, the initial volume variation is caused by osmotic pressure gradients between the two tanks.
- Model simulations adopting electrolyte with equal proton concentration or electrolyte with increased proton concentration result in a reduction of the initial capacity decay, highlighting the importance of migration to vanadium cross-over.
- With respect to commercial electrolyte, the adoption of electrolyte with equal proton concentration implies a reduction of battery capacity decay from 47.7% to 35.3% and an increase of coulombic and energy efficiency from 96.2% to 97.2% and from 79.9% to 84.4%, respectively. The volume variation is still present with a different intensity.
- With respect to commercial electrolyte, adopting electrolyte with increased proton concentration permits to reduce capacity decay to 36.3% and to increase coulombic and energy efficiency to 98.6% and 85%, respectively. Even the volume variation is reduced, but the one occurring during the first day of operation is still present due to the persistent initial osmotic pressure gradient.
- Combining electrolyte with high proton concentration and null osmotic pressure difference permits to completely mitigate electrolytes volume variation. Moreover, capacity decay is reduced down to 20.9%, while coulombic and energy efficiency increase to 98.9% and 83.4%, respectively. This electrolyte is effective with all the tested membranes, increasing the range of validity of the obtained results.

CRediT authorship contribution statement

F. Toja: Writing – original draft, Visualization, Validation, Methodology, Investigation, Formal analysis, Data curation, Conceptualization. **L. Perlini:** Validation, Methodology, Investigation, Data curation, Conceptualization. **D. Facchi:** Supervision, Resources. **A. Casalegno:** Supervision, Project administration. **M. Zago:** Writing – review & editing, Supervision, Project administration, Methodology, Funding acquisition, Conceptualization.

Declaration of Competing Interest

The authors declare that they have no known competing financial interests or personal relationships that could have appeared to influence the work reported in this paper.

Data availability

The data that has been used is confidential.

Acknowledgement

This work was partially funded by Solvay Specialty Polymers S.p.A. in the framework of the research project entitled: “Experimental characterization and modelling analysis of mass transport phenomena in vanadium redox flow batteries”.

Appendix A

Fig. A.1 reports the comparison of discharged capacity during 7 days of operation between the GfE commercial electrolyte [30] and the one prepared starting from $VOSO_4$, following the procedure explained in Section 2.2. In both the tests the adopted membrane was E98–05.

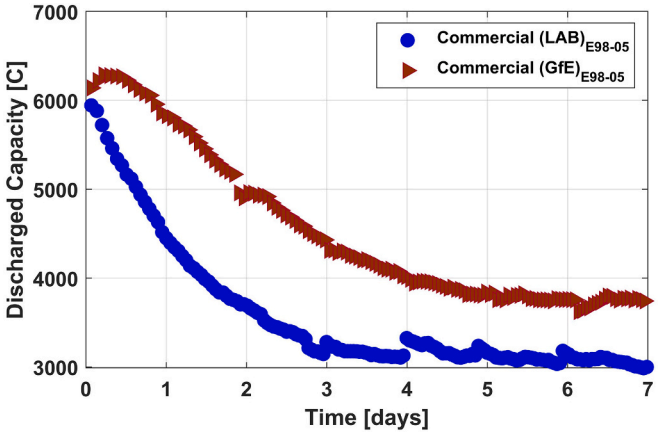

Fig. A.1. Comparison of discharged capacity with GfE commercial electrolyte and commercial electrolyte prepared starting from $VOSO_4$.

Appendix B

The initial volume of negative electrolyte with commercial electrolyte using E98–05 as separator (reported in Section 4.1.1) is shown in Fig. A. A clear volume variation takes place during the first charge/discharge cycle (Fig. B.1B), while no relevant volume variation is noticed along the rest of the first day of operation (Fig. B.1C).

Fig. B.1. Volume variation of negative electrolyte with commercial electrolyte adopting E98–05: A) beginning of the test; B) after one cycle; C) after one day.

Appendix C

The water transport between two tanks connected by a semipermeable membrane is evaluated in two cases. Fig. C.1-A1 reports the case of two tanks in which a different amount of solute moles is solved in water.

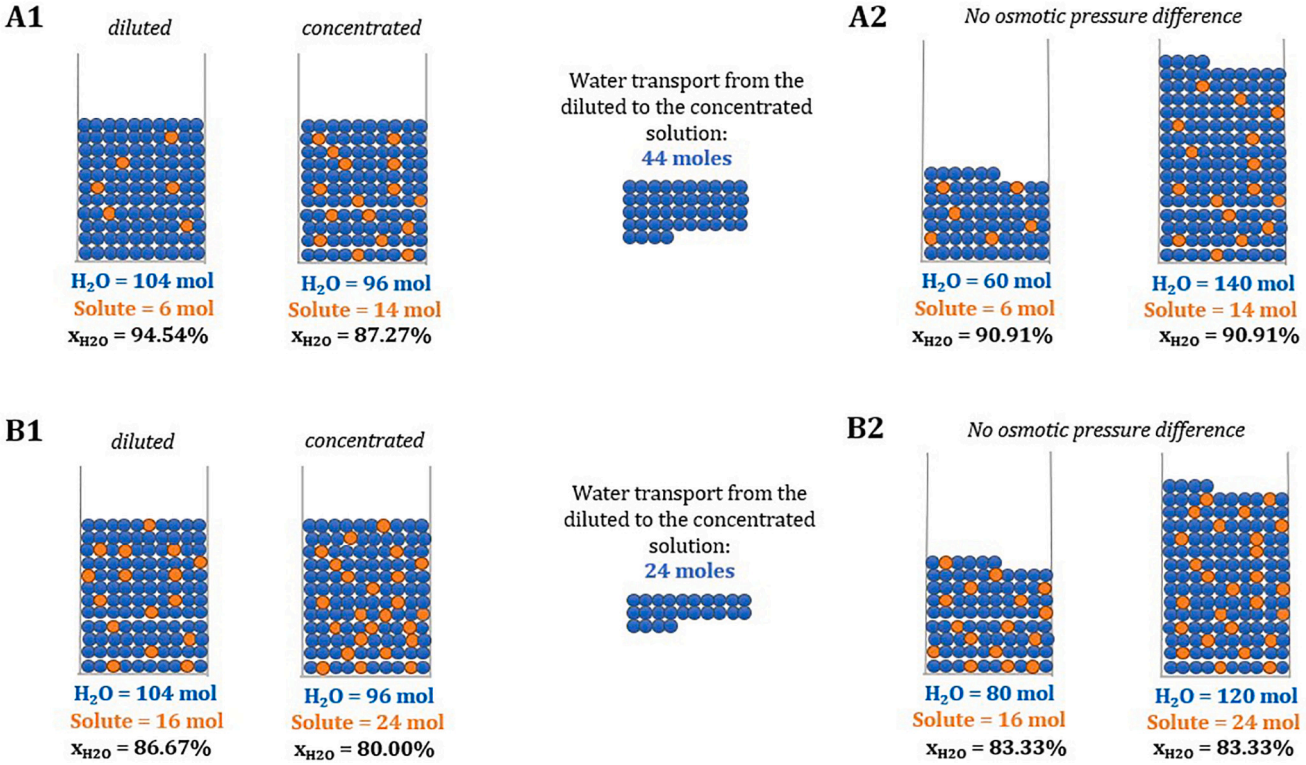

Fig. C.1. Water transport by osmosis: A) low solute concentration case; B) high solute concentration.

With *diluted* is indicated the tank in which is present a lower amount of solute and a higher amount of water. In the *concentrated* tank a higher quantity of solute is solved in a lower amount of water. The values of the water molar fractions and the osmotic pressure difference between the two tanks, computed with Eq. (63), are reported in Table C.1:

Table C.1
Water molar fraction and osmosis pressure difference between the diluted and the concentrated tanks.

Solution	diluted	concentrated	ΔP_{osm}[bar]
Case A1	94.54%	87.27%	−110.2
Case B1	86.67%	80.00%	−110.2

Assuming that the two tanks are connected with a semipermeable membrane that allows only the transport of water moles, the osmotic pressure difference existing between the two tanks, computed with Eq. (61), results in a net water transport from *diluted* to *concentrated,* that leads to the elimination of the osmotic pressure gradient between the two tanks. Fig. C.1–A2 shows that the transport of 44 mol is necessary to bring the two tanks at the same value of water molar fraction, thus eliminating the osmotic pressure difference. Fig. C.–B1 reports a case analogous to the one of Fig. C.–A1, with the difference that a higher quantity of solute is solved in the same amount of water moles of the two tanks, i.e. the two solutions are more

concentrated. The resulting ΔP_{osm} between the two sides, reported in Table C.1, is identical to the one of case A1. However, in the case of concentrated solutions, a lower water transport from diluted to concentrated tank is necessary to eliminate the osmotic pressure difference: as can be seen in Fig. C.–B2 its value is 24 mol, almost one half with respect to the previous case.

From this simple graphical and numerical demonstration, it clearly results that the net water transport existing between two tanks is lower when more concentrated solutions are used.

Appendix D

Figure and Figure report the trend of discharged capacity, electrolyte volume variation and mean efficiencies during 13 days of charge-discharge cycles using electrolytes with null osmotic pressure difference and increased proton concentration, adopting a VRFB with E87–05 and E98–09.

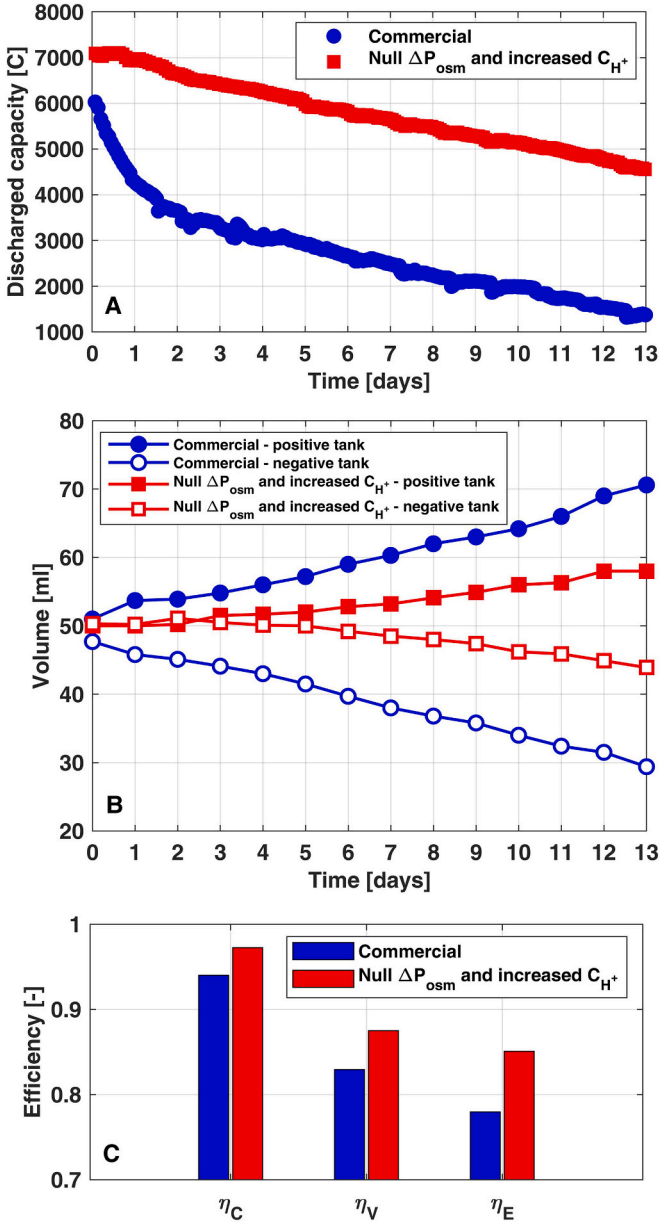

Fig. D.1. Charge-discharge cycles with E87–05 using electrolytes with null osmotic pressure difference and increased proton concentration: A) discharged capacity; B) electrolyte volume variation; C) mean efficiencies.

In both the cases, the adoption of this electrolyte considerably increases battery efficiencies and reduces capacity decay and volume variation, highlighting that the proposed electrolyte preparation is effective regardless the adopted membrane.

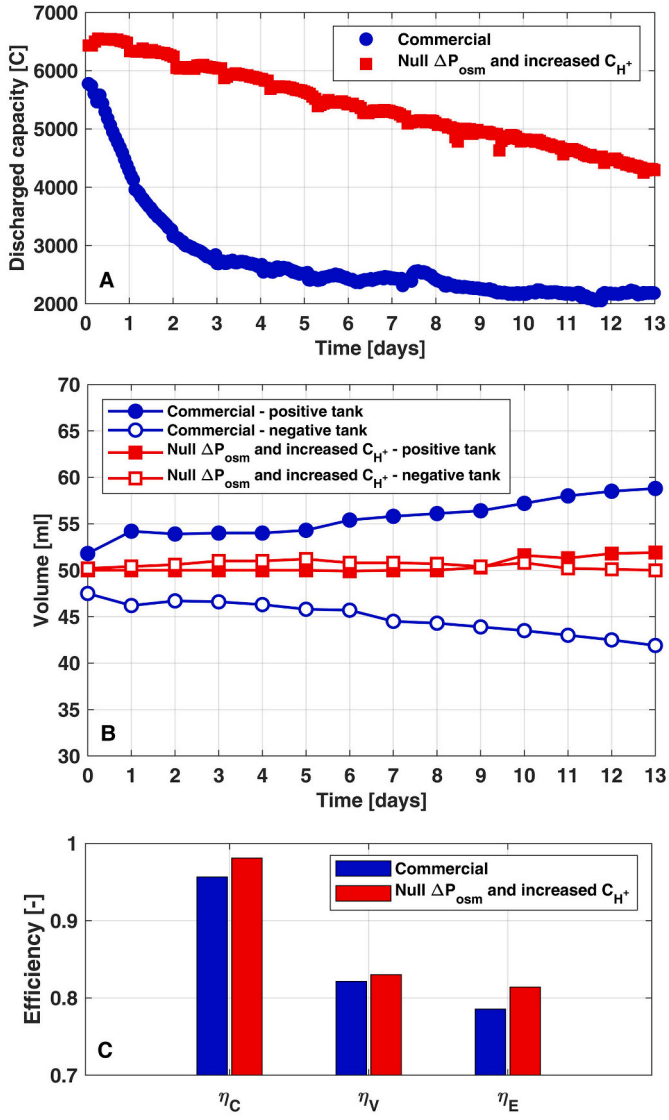

Fig. D.2. Charge-discharge cycles with E98–09 using electrolytes with null osmotic pressure difference and increased proton concentration: A) discharged capacity; B) electrolyte volume variation; C) mean efficiencies.

References

[1] Aneke M, Wang M. Energy storage technologies and real life applications – a state of the art review. Appl Energy 2016;179:350–77. https://doi.org/10.1016/j.apenergy.2016.06.097.

[2] Pugach M, Vyshinsky V, Bischi A. Energy efficiency analysis for a kilo-watt class vanadium redox flow battery system. Appl Energy 2019;253. https://doi.org/10.1016/j.apenergy.2019.113533.

[3] Jiang HR, Sun J, Wei L, Wu MC, Shyy W, Zhao TS. A high power density and long cycle life vanadium redox flow battery. Energy Storage Mater 2020;24:529–40. https://doi.org/10.1016/j.ensm.2019.07.005.

[4] Shi Y, Eze C, Xiong B, He W, Zhang H, Lim TM, et al. Recent development of membrane for vanadium redox flow battery applications: a review. Appl Energy 2019;238:202–24. https://doi.org/10.1016/j.apenergy.2018.12.087.

[5] Cecchetti M, Ebaugh TA, Yu H, Bonville L, Gambaro C, Meda L, et al. Design and development of an innovative barrier layer to mitigate crossover in vanadium redox flow batteries. J Electrochem Soc 2020;167:130535. https://doi.org/10.1149/1945-7111/abbbbb.

[6] Cecchetti M, Toja F, Casalegno A, Zago M. A comprehensive experimental and modelling approach for the evaluation of cross-over fluxes in vanadium redox flow battery. J Energy Storage 2023;68. https://doi.org/10.1016/j.est.2023.107846.

[7] Lei Y, Zhang BW, Zhang ZH, Bai BF, Zhao TS. An improved model of ion selective adsorption in membrane and its application in vanadium redox flow batteries. Appl Energy 2018;215:591–601. https://doi.org/10.1016/j.apenergy.2018.02.042.

[8] Zhang Y, Liu L, Xi J, Wu Z, Qiu X. The benefits and limitations of electrolyte mixing in vanadium flow batteries. Appl Energy 2017;204:373–81. https://doi.org/10.1016/j.apenergy.2017.07.049.

[9] Kapoor M, Beriwal N, Verma A. Maximizing durability of vanadium redox flow battery by evaluating electrolyte-repair-point. J Energy Storage 2020;32. https://doi.org/10.1016/j.est.2020.101759.

[10] Yuan XZ, Song C, Platt A, Zhao N, Wang H, Li H, et al. A review of all-vanadium redox flow battery durability: degradation mechanisms and mitigation strategies. Int J Energy Res 2019;43:6599–638. https://doi.org/10.1002/er.4607.

[11] Luo Q, Li L, Wang W, Nie Z, Wei X, Li B, et al. Capacity decay and remediation of nafion-based all-vanadium redox flow batteries. ChemSusChem. 2013;6:268–74. https://doi.org/10.1002/cssc.201200730.

[12] Rodby KE, Carney TJ, Ashraf Gandomi Y, Barton JL, Darling RM, Brushett FR. Assessing the levelized cost of vanadium redox flow batteries with capacity fade and rebalancing. J Power Sources 2020;460. https://doi.org/10.1016/j.jpowsour.2020.227958.

[13] Poli N, Trovò A, Fischer P, Noack J, Guarnieri M. Electrochemical rebalancing process for vanadium flow batteries: sizing and economic assessment. J Energy Storage 2023;58. https://doi.org/10.1016/j.est.2022.106404.

[14] T. Mohammadi, S.C. Chieng, M. Skyllas Kazacos B', Water transport study across commercial ion exchange membranes in the vanadium redox flow battery, 1997.

[15] Sukkar T, Skyllas-Kazacos M. Water transfer behaviour across cation exchange membranes in the vanadium redox battery. J Membr Sci 2003;222:235–47. https://doi.org/10.1016/S0376-7388(03)00309-0.

[16] Pugach M, Kondratenko M, Briola S, Bischi A. Zero dimensional dynamic model of vanadium redox flow battery cell incorporating all modes of vanadium ions

crossover. Appl Energy 2018;226:560–9. https://doi.org/10.1016/j.apenergy.2018.05.124.
[17] Yang XG, Ye Q, Cheng P, Zhao TS. Effects of the electric field on ion crossover in vanadium redox flow batteries. Appl Energy 2015;145:306–19. https://doi.org/10.1016/j.apenergy.2015.02.038.
[18] Lei Y, Zhang BW, Bai BF, Chen X, Zhao TS. A transient model for vanadium redox flow batteries with bipolar membranes. J Power Sources 2021;496. https://doi.org/10.1016/j.jpowsour.2021.229829.
[19] Knehr KW, Agar E, Dennison CR, Kalidindi AR, Kumbur EC. A transient vanadium flow battery model incorporating vanadium crossover and water transport through the membrane. J Electrochem Soc 2012;159:A1446–59. https://doi.org/10.1149/2.017209jes.
[20] Oh K, Moazzam M, Gwak G, Ju H. Water crossover phenomena in all-vanadium redox flow batteries. Electrochim Acta 2019;297:101–11. https://doi.org/10.1016/j.electacta.2018.11.151.
[21] Ashraf Gandomi Y, Aaron DS, Mench MM. Influence of membrane equivalentweight and reinforcement on ionic species crossover in all-vanadium redox flow batteries. Membranes (Basel) 2017;7. https://doi.org/10.3390/membranes7020029.
[22] Zheng Q, Li X, Cheng Y, Ning G, Xing F, Zhang H. Development and perspective in vanadium flow battery modeling. Appl Energy 2014;132:254–66. https://doi.org/10.1016/j.apenergy.2014.06.077.
[23] Wei Z, Siddique NA, Liu D, Sakri S, Liu F. Numerical study of effect of membrane properties on long-cycle performance of vanadium redox flow batteries. Adv Energy Res 2016;4:285–97. https://doi.org/10.12989/eri.2016.4.4.285.
[24] Shin J, Jeong B, Chinannai MF, Ju H. Mitigation of water and electrolyte imbalance in all-vanadium redox flow batteries. Electrochim Acta 2021;390. https://doi.org/10.1016/j.electacta.2021.138858.
[25] Shin J, Kim C, Jeong B, Vaz N, Ju H. New operating strategy for all-vanadium redox flow batteries to mitigate electrolyte imbalance. J Power Sources 2022;526. https://doi.org/10.1016/j.jpowsour.2022.231144.
[26] Wang Z, Guo Z, Ren J, Li Y, Liu B, Fan X, et al. An electrolyte with elevated average valence for suppressing the capacity decay of vanadium redox flow batteries. ACS Cent Sci 2023;9:56–63. https://doi.org/10.1021/acscentsci.2c01112.
[27] Chen L, Liu T, Zhang Y, Liu H, Ding M, Pan D. Mitigating capacity decay by adding carbohydrate in the negative electrolyte of vanadium redox flow battery. Energies (Basel) 2022;15. https://doi.org/10.3390/en15072454.
[28] Eifert L, Jusys Z, Behm RJ, Zeis R. Side reactions and stability of pre-treated carbon felt electrodes for vanadium redox flow batteries: a DEMS study. Carbon N Y 2020;158:580–7. https://doi.org/10.1016/j.carbon.2019.11.029.
[29] Vanadium Electrolyte Solution 1.6 M - Oxkem (n.d.), https://oxkem.com/product_pdfs/Vanadium%20electrolyte.pdf.
[30] Vanadium Electrolyte Solution 1.6 M - GfE (n.d.), https://www.gfe.com/02_produkte_loesungen/03_vanadium-chemikalien/PDB/Vanadium-Electrolyte-Solution-1.6-M-2012-114_V8.pdf.
[31] Schweiss R, Pritzl A, Meiser C. Parasitic hydrogen evolution at different carbon fiber electrodes in vanadium redox flow batteries. J Electrochem Soc 2016;163:A2089–94. https://doi.org/10.1149/2.1281609jes.
[32] Wei L, Zhao TS, Xu Q, Zhou XL, Zhang ZH. In-situ investigation of hydrogen evolution behavior in vanadium redox flow batteries. Appl Energy 2017;190:1112–8. https://doi.org/10.1016/j.apenergy.2017.01.039.
[33] Sun CN, Delnick FM, Baggetto L, Veith GM, Zawodzinski TA. Hydrogen evolution at the negative electrode of the all-vanadium redox flow batteries. J Power Sources 2014;248:560–4. https://doi.org/10.1016/j.jpowsour.2013.09.125.
[34] Liu H, Xu Q, Yan C, Qiao Y. Corrosion behavior of a positive graphite electrode in vanadium redox flow battery. Electrochim Acta 2011;56:8783–90. https://doi.org/10.1016/j.electacta.2011.07.083.
[35] Singh AK, Pahlevaninezhad M, Yasri N, Roberts EPL. Degradation of carbon electrodes in the all-vanadium redox flow battery. ChemSusChem. 2021;14:2100–11. https://doi.org/10.1002/cssc.202100082.
[36] Nourani M, Zackin BI, Sabarirajan DC, Taspinar R, Artyushkova K, Liu F, et al. Impact of corrosion conditions on carbon paper electrode morphology and the performance of a vanadium redox flow battery. J Electrochem Soc 2019;166:A353–63. https://doi.org/10.1149/2.1041902jes.
[37] Zago M, Casalegno A. Physically-based impedance modeling of the negative electrode in all-vanadium redox flow batteries: insight into mass transport issues. Electrochim Acta 2017;248:505–17. https://doi.org/10.1016/j.electacta.2017.07.166.
[38] Li Y, Sun L, Cao L, Bao J, Skyllas-Kazacos M. Dynamic model based membrane permeability estimation for online SOC imbalances monitoring of vanadium redox flow batteries. J Energy Storage 2021;39. https://doi.org/10.1016/j.est.2021.102688.
[39] Lei Y, Zhang BW, Bai BF, Chen X, Zhao TS. A transient model for vanadium redox flow batteries with bipolar membranes. J Power Sources 2021;496. https://doi.org/10.1016/j.jpowsour.2021.229829.
[40] Lei Y, Zhang BW, Bai BF, Zhao TS. A transient electrochemical model incorporating the Donnan effect for all-vanadium redox flow batteries. J Power Sources 2015;299:202–11. https://doi.org/10.1016/j.jpowsour.2015.08.100.
[41] Chen D, Hickner MA, Agar E, Kumbur EC. Selective anion exchange membranes for high coulombic efficiency vanadium redox flow batteries. Electrochem Commun 2013;26:37–40. https://doi.org/10.1016/j.elecom.2012.10.007.
[42] Messaggi M, Gambaro C, Casalegno A, Zago M. Development of innovative flow fields in a vanadium redox flow battery: design of channel obstructions with the aid of 3D computational fluid dynamic model and experimental validation through locally-resolved polarization curves. J Power Sources 2022;526. https://doi.org/10.1016/j.jpowsour.2022.231155.
[43] Oh K, Won S, Ju H. A comparative study of species migration and diffusion mechanisms in all-vanadium redox flow batteries. Electrochim Acta 2015;181:238–47. https://doi.org/10.1016/j.electacta.2015.03.012.
[44] Won S, Oh K, Ju H. Numerical analysis of vanadium crossover effects in all-vanadium redox flow batteries. Electrochim Acta 2015;177:310–20. https://doi.org/10.1016/j.electacta.2015.01.166.
[45] Lu MY, Yang WW, Deng YM, Li WZ, Xu Q, He YL. Mitigating capacity decay and improving charge-discharge performance of a vanadium redox flow battery with asymmetric operating conditions. Electrochim Acta 2019;309:283–99. https://doi.org/10.1016/j.electacta.2019.04.032.
[46] Agar E, Knehr KW, Chen D, Hickner MA, Kumbur EC. Species transport mechanisms governing capacity loss in vanadium flow batteries: comparing Nafion® and sulfonated Radel membranes. Electrochim Acta 2013;98:66–74. https://doi.org/10.1016/j.electacta.2013.03.030.
[47] Boettcher PA, Agar E, Dennison CR, Kumbur EC. Modeling of ion crossover in vanadium redox flow batteries: a computationally-efficient lumped parameter approach for extended cycling. J Electrochem Soc 2016;163:A5244–52. https://doi.org/10.1149/2.0311601jes.
[48] Wang Y, Hao L. Effect of membrane properties on ion crossover in vanadium redox flow batteries. J Electrochem Soc 2019;166:A3784–95. https://doi.org/10.1149/2.1011915jes.
[49] Hao L, Wang Y, He Y. Modeling of ion crossover in an all-vanadium redox flow battery with the interfacial effect at membrane/electrode interfaces. J Electrochem Soc 2019;166:A1310–22. https://doi.org/10.1149/2.1061906jes.
[50] Feher J. Osmosis and osmotic pressure. In: Quantitative human physiology. Elsevier; 2017. p. 182–98. https://doi.org/10.1016/b978-0-12-800883-6.00017-3.
[51] Wyckoff RD, Botset HG, Muskat M, Reed DW. The measurement of the permeability of porous media for homogeneous fluids. Rev Sci Instrum 1933;4:394–405. https://doi.org/10.1063/1.1749155.
[52] Rahman F, Skyllas-Kazacos M. Solubility of vanadyl sulfate in concentrated sulfuric acid solutions. 1998.